The Fully Nonlinear Stratified Geostrophic Adjustment Problem

Aaron Coutino[1] and Marek Stastna[1]

[1]University of Waterloo, Department of Applied Mathematics

Correspondence to: Aaron Coutino (acoutino@uwaterloo.ca)

Abstract. The study of the adjustment to equilibrium by a stratified fluid in a rotating reference frame is a classical problem in geophysical fluid dynamics. We consider the fully nonlinear, stratified adjustment problem from a numerical point of view. We present results of smooth dam break simulations based on experiments in the published literature, with focus on both the wave trains that propagate away from the nascent geostrophic state and the geostrophic state itself. For the Rossby number range considered the rank ordered solitary wave trains and undular bores of the non-rotating adjustment problem break down into a leading packet-like disturbance, a trailing tail, and a geostrophic state with superimposed decaying inertial oscillations. Variations in Rossby number are considered and demonstrate that two wave trains emanate from the inertial oscillations of the geostrophic state itself. For wide initial states, the wave train that initially propagates into the nascent geostrophic state is clearly apparent. We quantify the strength of the inertial oscillations of the geostrophic state and find results that are in agreement with hydrostatic, shallow water equation-based theory in the literature. It is found that the leading wave packet never completely separates from the trailing tail in this case, in agreement with previously published work. Finally, we investigate whether the wave train and geostrophic state exhibit nonlinear effects, and find that for low (high) Rossby numbers, nonlinear effects in the geostrophic state (wave train) are significant.

1 Introduction

Geostrophic balance, namely the balance between the pressure gradient and the Coriolis pseudo force, is observed to hold to a good approximation for many large-scale motions in the atmosphere and the ocean. The process through which some disturbed state reaches this balance is called geostrophic adjustment. This problem was first considered by Rossby (1937). Using conservation of momentum and mass, he derived the geostrophic steady state corresponding to an initial perturbation. In the original publication, Rossby noted that the final state of the system possessed less energy than the initial state. The cause of this difference was identified by Cahn (1945), who showed that the end state is reached via inertial oscillations, which disperse energy through waves. Since then, numerous papers have used a variety of methods such as asymptotic expansions and numerical integration to solve this linear problem. There has been a great deal of published work on the linear problem (Ou (1984); Gill (1976); Middleton (1987); Washington (1964); Mihaljan (1963)), but little on the fully nonlinear one. This is partly because nonlinear problems rarely yield analytical solutions in closed form, and partly because numerical methods applied to the problem must accurately resolve multiple length scales.

Kuo and Polvani (1999), a key paper in the study of the nonlinear problem, considered the adjustment problem in the context of

the single layer shallow water equations in one dimension. The authors built on the results of Killworth (1992), and performed a numerical analysis of the fully nonlinear problem with 'dam break' initial conditions (see Gill (1982)). The authors found that the nonlinearity and rotation led to bore generation, with the bores dissipating energy as they propagated away from the geostrophic state. Since the nonlinear shallow water equations neglect non-hydrostatic dispersion, these bores manifested as shock-like fronts. This is in contrast to the non rotating stratified adjustment problem which leads to the generation of either a rank-ordered train of internal solitary waves, or an undular bore. Indeed, in this dispersive system, for the majority of parameter space, breaking is not observed. The authors also found that the inertial oscillations within the geostrophic state can persist for long times and are highly dependent on the initial conditions. In their analysis of the energy within the geostrophic state, the authors found that the ratio of change in kinetic energy (ΔKE) to change in potential energy (ΔPE) tended to $\frac{1}{3}$ which is the theoretically predicted value for both the linear and nonlinear problems (see Boss and Thompson (1995)). However, Kuo and Polvani showed that even for late times, the energy ratio fluctuated by up to 30% around the $\frac{1}{3}$ value.

The nonlinear effects on the rotating adjustment problem have been investigated analytically using multiple scale perturbation analysis of the shallow-water and full stratified equations. In part one of a two part paper series Zeitlin et al. (2003a) perturb the rotating shallow-water equations using Rossby number as their small parameter. The authors proceed to confirm that a slow-fast splitting is possible, with the slow state largely remaining in geostrophic balance and largely unaffected by the fast state. In the waves that are generated Zeitlin et al. observe shock formation and present a semi-quantitative criteria for this, based on the initial conditions. In the second paper, Zeitlin et al. (2003b), the authors generalize their results to the case of continuous stratification and also consider two layer and quasi-two layer stratifications. Zeitlin et al. perform a number of asymptotic expansions for different initial isopycnal deviation regimes. They conclude that for large deviations the model strongly depends on the ratio of the layer depths and that the waves produced from the initialization obey a Schrödinger-type modulation equation. For small deviations the waves generated are not impacted by the geostrophic state which is left to evolve according to the standard quasi-geostrophic (QG) equations.

Rotation-influenced nonlinear waves have also been considered using a model nonlinear wave equation; in this case a member of the Korteweg de Vries (KdV) family of equations . The KdV equation is the simplest model equation that allows for a balance between nonlinear and dispersive effects, with a rich mathematical structure which makes predictions of the evolution of an initial state that are remarkably robust in both a laboratory and field setting (see Johnson (1997)). A rotation-modified version of the KdV equation was first derived by Ostrovsky (see Grimshaw et al. (2012) for an in-depth discussion of the equation properties and references to the Russian literature). This new equation was subsequently analysed both through theoretical solutions found by asymptotic expansions and through numerical solutions. Investigation of the model equations revealed that the precise balance between nonlinearity and dispersion that leads to the traditional soliton solution of the KdV-equation is destroyed by the addition of rotation, and that over time the soliton breaks down into a nonlinear wave packet (Grimshaw and Helfrich (2008)). This hypothesis was later supported by experimental results, (Grimshaw et al. (2013)). From a theoretical point of view, Grimshaw and Helfrich (2008) also found that the extended nonlinear Schrödinger (NLS) equation provides a good qualitative description of the wave packet. While the mathematical developments of the rotation-modified theory are substantial, it is also true that this theory has a number of pathologies not observed in the non-rotating KdV-based theory,

which in itself has been shown to misrepresent aspects of large amplitude solitary waves (Lamb (1997) is one of many papers to discuss some of these discrepancies).

Work has also been performed using models with higher order nonlinearity (Helfrich (2007)) but weak nonhydrostatic effects, as well as with the full set of stratified Euler equations (Stastna et al. (2009)). Both of these studies considered the breakdown of an initial solitary wave in the presence of rotation. Helfrich suggested that the initial solitary wave breaks down into a coherent leading wave packet with a trailing tail of waves. Stastna et al. suggested that for large amplitude, exact internal solitary waves that are solutions to the Dubreil-Jacotin-Long (DJL) equation, Helfrich's result was observed for artificially high rotation rates, while rotation rates typical of mid-latitudes led to a disturbance that never fully separated from the trailing tail. Despite differences in details, the qualitative features observed in both studies were quite similar. Additionally, they also performed collision experiments, finding that the packets that emerge from the initial solitary waves can merge during collisions, and hence do not interact as classical solitons. Finally, Stastna et al. also found that by increasing the width of a flat-crested wave, more energy was deposited into the tail. It remains to reconcile the two sets of results in detail, likely by systematically reducing the solitary wave amplitude used as an initial condition.

In this paper, we present the results of high resolution simulations of the geostrophic adjustment of a stratified fluid with a single pycnocline on an experimental scale. Our simulations consider the full set of stratified Euler equations using a pseudo-spectral collocation method. We begin by providing and reviewing the non-rotating case and the changes that arise when polarity of the initial condition is changed. Next we present the general evolution of the rotating case using a 'base' case comparable to one of the cases presented in Grimshaw et al. (2013). The rotation rate (i.e., Rossby number) is then varied and the resulting changes are documented. Simulations with the same Rossby number but different initial widths and rotation rates are presented, and their similarities highlighted. We then focus on the geostrophic state, specifically examining the change in kinetic energy and the change in potential energy for different initial widths. Using the potential energy we are able to clearly show the generation and reflection of a leftward wave from the initial condition. This wave train interacts with the geostrophic state, reflects off the left wall of the domain and then continues to propagate rightward across the tank. This is of potential interest to future experiments. We then focus on the change between $Ro < 1$ and $Ro > 1$, specifically the change in dynamics of the wave packet in each regime. We conclude by considering the nonlinear effects that arise from changes in polarity and changes in amplitude, including a very small amplitude case expected to reflect the results of linear theory. We find that nonlinear effects are significant in either the geostrophic state or the wave train for all Rossby numbers tried.

2 Methods

For the following numerical simulations, the full set of stratified Euler equations for an incompressible fluid were used, though no span-wise variations were considered. Rotation was incorporated using an f-plane approximation and the non-traditional Coriolis terms were dropped. For a review of the effects of the non-traditional Coriolis terms see Gerkema et al. (2008). The x-axis is taken as parallel to the flat ocean bottom with the z-axis pointing upward ($\hat{k}$ is the upward directed

unit vector). The origin is placed in the bottom left corner so that both axes are positive. The Euler equations for velocity $\boldsymbol{u} = [u(x,z,t), v(x,z,t), w(x,z,t)]$, density $\rho(x,z,t)$, and pressure $P(x,z,t)$ are,

$$\frac{D\boldsymbol{u}}{Dt} + (-fv, fu, 0) = -\boldsymbol{\nabla} P - \rho' g\hat{k} + \nu\nabla^2\boldsymbol{u}, \tag{1}$$

$$\nabla \cdot \boldsymbol{u} = 0, \tag{2}$$

$$\frac{D\rho}{Dt} = 0. \tag{3}$$

In accordance with convention, we have divided the momentum equation by the constant reference density ρ_0 and absorbed the hydrostatic pressure into the pressure P. We make the Boussinesq approximation for density and write $\rho = \rho_0(1 + \bar{\rho}(z) + \rho'(x,z,t))$, where $\bar{\rho}$ is the background density profile and ρ' is considered a small perturbation. Due to our interest in the wave dynamics in the main water column, as opposed to details of the boundary layer dynamics, we impose free slip boundary conditions at the top and bottom of our domain. This will also ensure that the boundary layer does not play a significant role in the simulations on which we report. The walls allow us to mimic a lock-release set up that is used to create waves in many laboratory set ups (Carr and Davies (2006); Grue et al. (2000); Helfrich and Melville (2006)). We have chosen to neglect the span-wise dimension (y), as the lab results in Grimshaw et al. (2013) were performed away from any side boundaries and the authors elected to neglect any curvature from the waves created. For the energy calculations we follow the procedure from Lamb and Nguyen (2009). Specifically we use (a discrete version) of their equation (14) to calculate APE within a fixed length. For the background density we followed the recommendation from Lamb and Nguyen (2009) and elected to use the density profile from the far right-hand side of the tank, since little mixing of the pycnocline is observed. Tests using a sorting of the density field suggest this is an acceptable choice.

In the following set of experiments the two dimensionless numbers which are dynamically important are the Rossby number and the Reynolds number. The Rossby number is defined as $Ro = \frac{U}{fL}$, where U is the typical wave speed, L is the typical length scale and f is the rotation rate. This reflects a ratio of the inertia term to the Coriolis pseudoforce term (henceforth just force). When the Coriolis force dominates, the fluid can reach a balance between the rotation and pressure terms, i.e., geostrophic balance. The Reynolds number is given as $Re = \frac{UL}{\nu}$, where U and L are the same as for Ro and ν is the kinematic viscosity. In addition to these traditional dimensionless numbers we also define a nonlinearity parameter α found in Kuo and Polvani (1997), defined as $\alpha = \frac{\eta}{H_1}$, where η is the height of the displacement in isopycnals and H_1 is the height of the undisturbed fluid column. This parameter can be used to modify the strength of the nonlinearity, and is well suited for shallow water equations. For the full set of Euler equations some ambiguity is introduced by the vertical structure of the stratification and the initial perturbation. Nevertheless, we have found α to be a useful parameter, likely since the disturbances in our simulations are dominated by mode-1 waves.

The numerical simulations presented here were performed using an incompressible Navier Stokes equation solver which implements a pseudo-spectral collocation method (SPINS), presented in Subich et al. (2013). The solver uses spectral methods resulting in the order of accuracy scaling with the number of grid points. To deal with the build up of energy in the high wave numbers an exponential filter is used after a specific wave number cut off.

We computed a series of 2D lab scale numerical simulations on a similar scale to the physical experiments presented in Grimshaw and Helfrich (2008), which were performed using the $13\mathrm{m}$ diameter rotating platform at the LEGI-Coriolis Laboratory in Grenoble. Motivated by the results presented in Stastna et al. (2009), a domain four times larger than the physical tank ($Lx = 52\mathrm{m}$) was used, as the $13\mathrm{m}$ is an insufficient length when considering lower (closer to physical) rotation rates. In addition to this it was decided to change the tank depth to a more evenly divisible $0.4\mathrm{m}$ (from a laboratory value of $0.36\mathrm{m}$). The density difference was set to 1% to match Grimshaw and Helfrich. A schematic diagram of the tank set-up is provided in Fig. 1. The different physical parameters related to the initial set-up are illustrated in this figure.

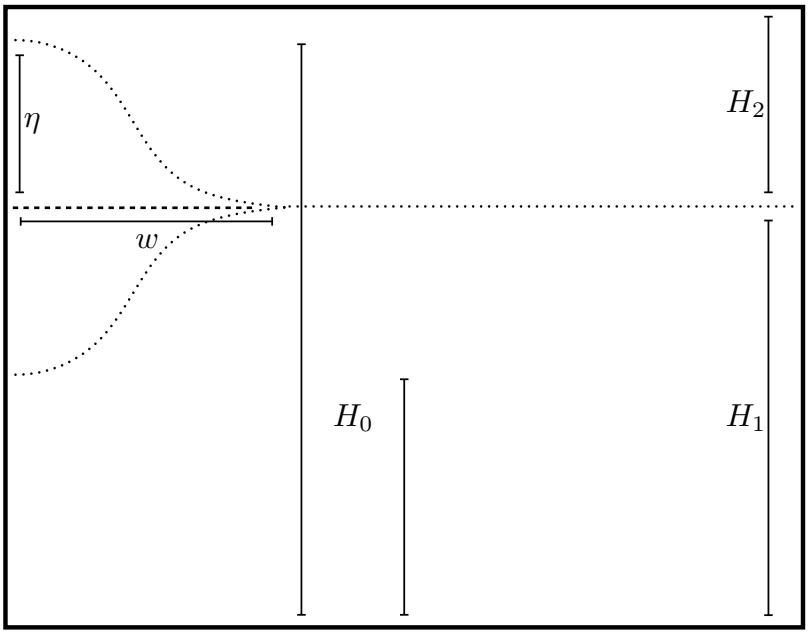

Figure 1. A schematic of the tank simulation set-up which illustrates the different parameters. The dotted line represents the isopycnal found at the centre of the pycnocline on the far right of the domain. The largest deflection (both polarities are shown in the figure) occurs at the left end point of the domain. H_1 and H_2 represent the depth of fluid below and above the centre of the undisturbed pycnocline, respectively. H_0 is the maximum or minimum height of the pycnocline created by the initial conditions. η is the isopycnal displacement. w is the width of the initial condition defined from the left-hand wall to where the pycnocline reaches within 1% of the undisturbed height.

8192 grid points were used to resolve the $52\mathrm{m}$ length of the tank and 192 points were used for the $0.4\mathrm{m}$ height, providing a $0.006\mathrm{m}$ horizontal resolution and $0.002\mathrm{m}$ vertical resolution. To easily compare these numerical results to the experimental values in Grimshaw et al., our rotation rate was based on their lowest presented value of f, which had a value of $0.105\mathrm{s}^{-1}$. It was also decided to base the initial perturbation width w_0 on twice the Rossby radius of deformation so as to allow for a neater examination of the parameter space. In each of the simulations, the initial conditions were given by a quiescent fluid, and a

density field defined via the isopycnal displacement η,

$$\rho(x,z,t=0) = \bar{\rho}(x,z-\eta) = -0.005\rho_0 \tanh\left(\frac{z-\eta-0.3}{0.01}\right),$$

$$\eta = \pm 0.05 \exp\left[-\left(\frac{x}{w}\right)^8\right],$$

where w is the half width of the initial perturbation and the sign changes correspond to changes in jump orientation.

3 Results

In this section we present the results of multiple numerical simulations. Parameters were primarily modified by changing either the initial width of the perturbation or by changing the rotation rate. Using the initial width as the typical length scale, $L = w$, we are thus varying the Rossby number. The resulting values of Ro are shown in Table 1. Across all the cases, the depth does not change, and hence neither does the two-layer linear long wave speed $U = \sqrt{g\frac{\Delta\rho}{\rho_0}\frac{H_1 H_2}{H_1+H_2}} = 0.0858\,\mathrm{m\,s^{-1}}$, where $g = 9.81\,\mathrm{m\,s^{-2}}$, $\Delta\rho = 10\,\mathrm{kg\,m^{-3}}$, $\rho_0 = 1000\,\mathrm{kg\,m^{-3}}$, $H_1 = 0.3\mathrm{m}$ and $H_2 = 0.1\mathrm{m}$. This implies that there are two readily accessible ways to create a situation with the same Rossby number. Using the same wave speed and length scales as for the Rossby number, the corresponding Reynolds numbers are presented in Table 2. The kinematic viscosity was the same for all simulations, $\nu = 1e^{-6}\,\mathrm{m^2\,s^{-1}}$. It is also possible to define a Reynolds number based on the channel depth, $L = 0.4\mathrm{m}$, providing a corresponding $Re = 3.43 \cdot 10^5$. This would be the same for all cases since domain depth does not change. Several additional experiments were carried out changing the initial wave amplitude which results in different 'nonlinearity' parameters. For the initial amplitude of $\eta = 0.05\mathrm{m}$ and undisturbed pycnocline height $H_0 = 0.3\mathrm{m}$ we have $\alpha = 0.1667$. For the cases where amplitude is halved and quartered corresponding alpha values are $\alpha = 0.0833$ and $\alpha = 0.0416$. The initial value of $\alpha = 0.1667$ allows for an easy comparison to many of the figures in Kuo and Polvani which are based on a value of 0.1. In addition to the simulations above, another set of simulations were performed using the opposite polarity of the initial disturbance. These opposite polarity simulations correspond exactly to the cases seen in Table 1, the only difference being the sign in the isopycnal displacement used in the initial conditions.

Several simulations were also performed on an extra-long tank to investigate the long-time results of adjustment. For these simulations the tank length was $L = 260\mathrm{m}$ and the number of horizontal grid points was increased to 16384, providing a $0.0158\mathrm{m}$ resolution. The vertical height and grid points were kept the same from the smaller case.

Unless otherwise stated the following scaling is used for all figures: $T = 1/f$, $L_z = Lz$ and $L_x = Ro_r$ where $Ro_r = \frac{U}{f}$ is the Rossby radius of deformation and $Lz = 0.4\mathrm{m}$ is the depth of the tank. For kinetic energy, we scale by the maximum kinetic energy *to show relative changes*. For convenience, we report both physical and dimensionless time in the figure captions.

3.1 Non-rotating cases

We begin by reproducing the results of the adjustment problem without rotation. The solution to this problem is well known, though we are not aware of any references that present the result in detail. We thus state the result, with a numerical example, and briefly outline the weakly nonlinear theory behind it. Non-rotating adjustment yields either a rank ordered train of

solitary waves, or an undular bore forming from the initial disturbance, depending upon the polarity of the initial disturbance. Examples of these two cases are shown in Fig. 2. Since there is no rotation, the advective time-scale was chosen,$T = L/U$, to nondimensionalize time, with the initial width $w = \frac{1}{2}w_0$ chosen for the typical length-scale. The stark difference between these cases is readily apparent in both types of plots.

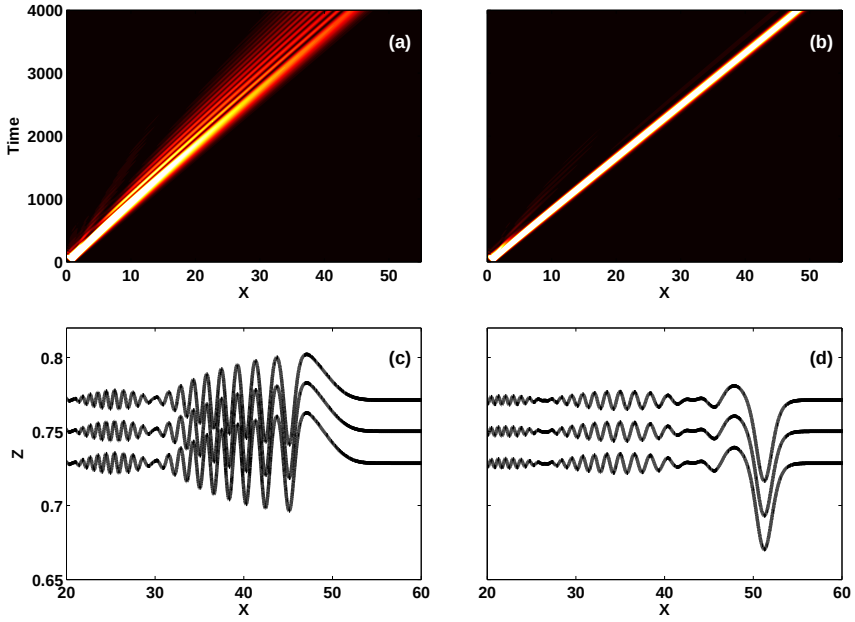

Figure 2. A space-time filled contour plot of vertically integrated kinetic energy and density isocontours at $t = 450\text{s}(4275)$ showing the differences between the positive and negative polarity initial conditions with $w = \frac{1}{2}w_0$. (a) and (c) correspond to the positive polarity case while (b) and (d) to the negative case.

The result may be understood in terms of KdV theory. Using the notation of Lamb (1997) The KdV equation corresponding to rightward propagating waves reads

$$B_t = -cB_x + 2cr_{10}BB_x + r_{01}B_{xxx}, \tag{4}$$

where c is the linear longwave speed, r_{10} is the nonlinearity coefficient, and r_{01} is the dispersive coefficient. The numerical value for c is computed from the linear longwave eigenvalue problem (Lamb's equation 8a), while r_{10} and r_{01} are computed from the integral expressions involving the eigenfunctions of the same problem (Lamb's equations 10a and 10b). The dispersive coefficient is always negative, while the nonlinear coefficient switches sign depending on the functional form of the stratification. In the case of a two-layer flow exact expressions can be derived. Solitary wave solutions of (4) are of the classical sech^2 form. The propagation speed equals the linear long wave speed to leading order, with a nonlinear correction that is proportional to amplitude and r_{10} (Lamb's equation 17). Thus the sign of r_{10} also determines solitary wave polarity. In the

absence of background shear currents this implies that stratifications centered above (below) the mid-depth yield solitary waves of depression (elevation). All numerical experiments performed with exact solitary waves computed using the DJL equation that we are aware of match the predictions of the KdV theory presented above, as far as solitary wave polarity is concerned. Of course, KdV theory is not necessarily a quantitatively accurate predictor of the structure of large solitary waves (Lamb (1997) is one of many papers to discuss some of the discrepancies).

3.2 General evolution

Comparing the value of the Rossby number in our cases to those discussed in Grimshaw et al. (2013), we find that their case with a rotation rate of $0.105\mathrm{s}^{-1}$ had a corresponding Rossby number of 0.667. Therefore, we use the $f = f_0$ and $w = w_0$ case as our baseline as it has $Ro = 0.5$ which is in the same regime as their number. Snapshots of the time evolution for this case are provided in Fig. 3.

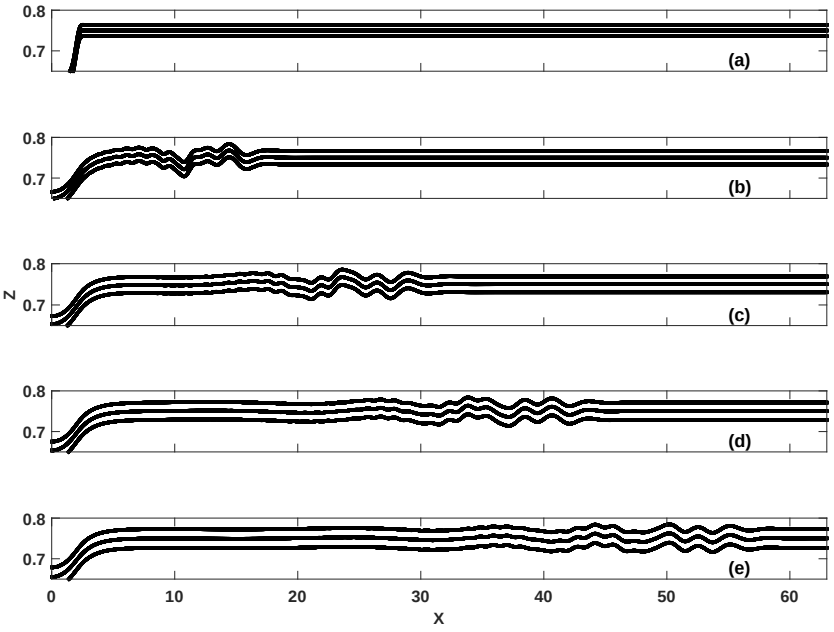

Figure 3. A line plot of density contours which show the time evolution of the waves generated from our 'base' case of $f = f_0$ and $w = w_0$ (so $Ro = 0.5$). (a) corresponds to $t = 0\mathrm{s}(0)$, (b) to $t = 150\mathrm{s}(15.75)$, (c) to $t = 300\mathrm{s}(31.5)$, (d) to $t = 450\mathrm{s}(47.25)$ and (e) to $t = 600\mathrm{s}(42)$.

Observing the structure that appears throughout the time series, we argue that these waves closely resemble a modulated wave packet as presented in Grimshaw et al. (1998), instead of the rotation modified bore seen in Kuo and Polvani (1997). When comparing to the work done by Kuo and Polvani, we first note that for our simulations the nonlinear parameter is quite small at $\alpha \approx 0.166$. However, their work suggests that even for this small value and smooth initial condition breaking will still

occur. The present simulations were carried out with the full set of Euler equations. As such, the dispersion that is neglected in the shallow water equations used by Kuo and Polvani becomes important when the wave front steepens. Dispersion breaks the front down into a train of smaller waves and eliminates shock formation. In addition to the change in steepening dynamics, the initially localized waves disperse over time, yet are observed to remain bound together (corresponding to the width of the packet envelope). For this reason we find that the modulated wave packet is a better description for these dynamics.

While the base case of Fig. 3 allows us to easily compare to the results from the LEGI-Coriolis tank with its relatively high rotation rate, in order to compare to what is observable in coastal waters or large lakes, we must consider lower rotation rates. While still being constrained by the size of our extended tank, it was decided to focus on a half and a quarter of the original rotation rate. Fig. 4 shows space-time plots of the vertically-integrated kinetic energy for these three rotation rates, with the initial width held the same at $w = w_0$. Fig. 4(a) corresponds to the base case in Fig. 3, while (b) to $f = \frac{1}{2}f_0$, and (c) to $f = \frac{1}{4}f_0$. Comparing to Table 1 we see that these cases have $Ro = \frac{1}{2}$, $Ro = 1$ and $Ro = 2$ respectively. In all cases, we can easily identify the geostrophic state that forms from the initialization near the left hand boundary of the model tank and observe that it oscillates, or pulsates, in time. This is in qualitative agreement with the results from Kuo and Polvani. These pulses are particularly evident in (a) and (b). Comparing the three plots we see that with the decrease in rotation rate we shift the location where, and the time when, the most energetic waves are ejected from the pulsating, geostrophic region. In Fig. 4(c) the kinetic energy is ejected almost immediately, and by the time the second pulse is visible in the geostrophic region the wave packet is well away from the left boundary. As the wave propagates away, it develops a clear wave packet structure which can be easily identified in the space-time plots. In Fig. 4(b) we see that the strongest kinetic energy propagates away from the second half of the initial pulse, but also develops a packet structure as it moves away from the geostrophic region. Differences arise when we look at (a), which has the highest rotation rate, where a small packet is generated however it is forms from the second pulse. Note for this case that by $t = 286\text{s}(30)$ the kinetic energy stops reaching a significant level within the packet. As expected, reducing the rotation rate leads to a weaker geostrophic state and more energy in the initial pulse of kinetic energy.

The cases where the rotation rate or initial width was varied, can both be interpreted as changing the Rossby number. With this in mind we investigate the results of keeping the Rossby number constant across changes in rotation by making a corresponding change in the initial width.

Figure 5 shows the space-time plots of kinetic energy for the same Rossby number formed using different combinations of rotation rate and initial width. The top three panels show the full evolution of the cases while the bottom three show a scaled version of the panel above. We have calculated the vertically integrated kinetic energy across the entire domain. The most striking feature of the top three panels in the figure is that dynamically they look the same, we have a primary, energetic wave packet produced from the first pulse of the geostrophic state, and this packet propagates away without very much spreading. We can also see that the oscillations of the geostrophic state remain quite evident for later times. The bottom three panels show rescaled plots and the similarities between the cases are immediately visible. The geostrophic state looks almost identical between the three cases. The inertial oscillations occur at nearly the same location in scaled space and have nearly the same intensity. While looking roughly similar, some differences arise in the wave train that is ejected. Specifically, we can see that the number and duration of the peaks of the wave train are different across the three cases, especially between (d) and (e).

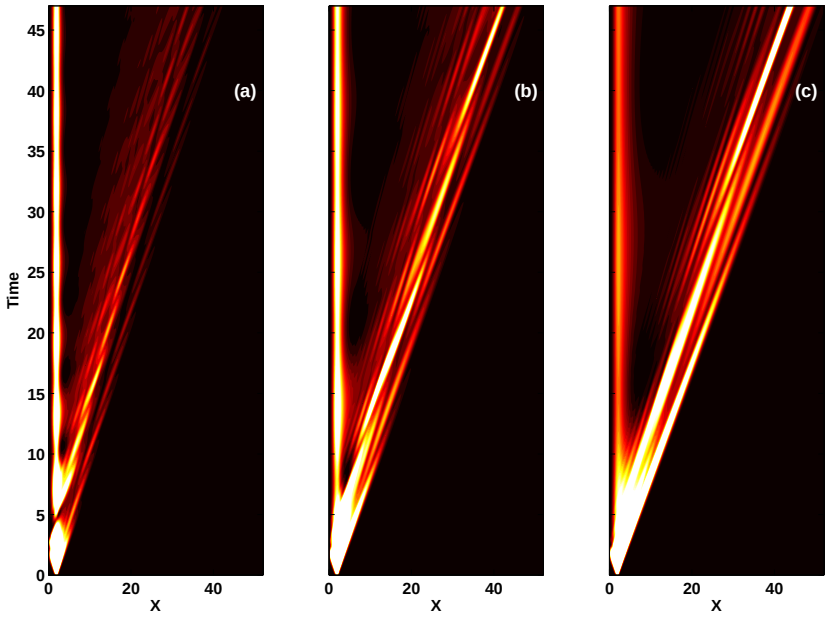

Figure 4. A space-time plot of the vertically integrated kinetic energy (scaled by its maximum value) for different values of f while w is held constant. (a) corresponds to the $f = f_0$ ($Ro = 0.5$) case, (b) corresponds to the $f = \frac{1}{2} f_0$ ($Ro = 1$) case and (c) to the $f = \frac{1}{4} f_0$ ($Ro = 2$) case.

3.3 The geostrophic state

In the rotation modified adjustment problem there are two dominant features, the geostrophic state that is left over from the initial conditions and the train of Poincaré waves which carries energy away from it. For this section we will focus on the dynamics, and changes, of the geostrophic state.

Figure 6 shows space-time plots of vertically-integrated kinetic energy for five cases of different initial widths where the rotation rate has been held constant at $f = f_0$. These cases have Rossby numbers 2, 1, $\frac{1}{2}$, $\frac{1}{4}$ and $\frac{1}{8}$ for (a), (b), (c), (d), and (e), respectively. This figure extends the trend seen in Fig. 4, where in this case increasing the initial width modifies the temporal phase of the geostrophic state's oscillation that leads to the wave packet generation. In particular, the generation occurs during the onset of the first pulse in (a) and shifts to the middle of the fourth pulse in (e). We can also note from this figure that as the initial width is increased, more energy is trapped in the geostrophic state, so that in (e) almost no energy is ejected via the packet. Notice that as we increase the width of the initialization the shape of the first pulse in kinetic energy changes as well. The wedge shape is created by the generation of waves in both directions, where the left-propagating wave reflects off the left-hand wall. For cases (a)-(c) the leftward propagating wave reflects off the wall and immediately interacts with the first pulse of the geostrophic state giving a lopsided wedge shape for the kinetic energy of the pulse. For the later two cases ((d)

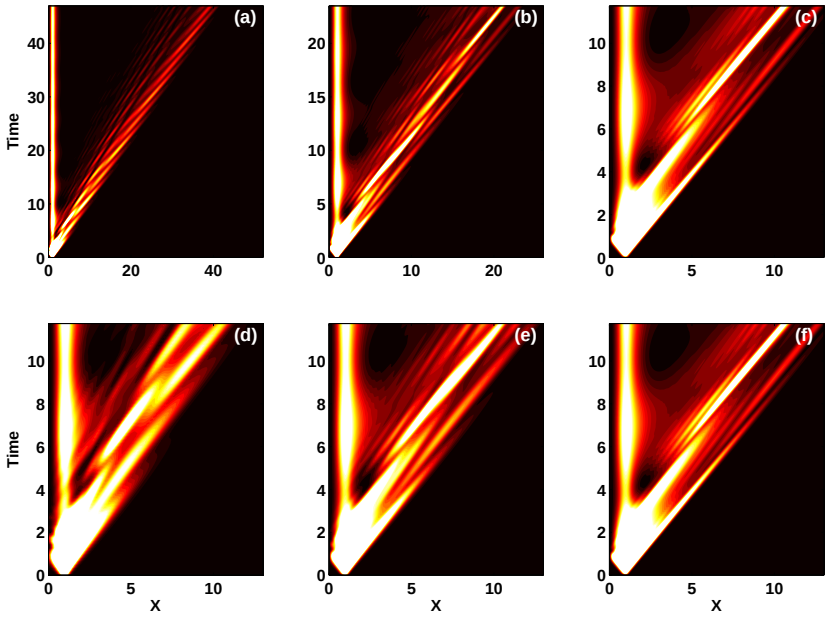

Figure 5. A space-time plot of kinetic energy. The different columns correspond to different combinations of f and w used to form a value of $Ro = 1$. (a) $f = f_0$ and $w = \frac{1}{2}w_0$, (b) $f = \frac{1}{2}f_0$ and $w = w_0$ and (c) $f = \frac{1}{4}f_0$ and $w = 2w_0$. The second row corresponds to the same case as the first columns but the aspect ratio has been scaled by the change in rotation rate.

and (e)), we can see the full arrow shape in the energy that forms from the propagation of the waves in two directions, at these width the reflection of the leftward wave takes enough time that it does not interact with the first pulse, but rather with later ones.

To further investigate the geostrophic state and to compare to with previously published work, we have computed the ΔPE and ΔKE within the geostrophic state compared to the initialization for the cases in Fig. 6, this is presented in Fig. 7. We have defined the geostrophic state as twice the distance from the left-hand wall to the maximum in kinetic energy. Due to the nature of our initial conditions, namely that we start with a smooth transition and still fluid, we cannot compute $\Delta PE/\Delta KE$ since the potential energy may be zero since it can reach its initial starting point. For this reason we have presented the differences separately ((a) for ΔPE and (b) for ΔKE). The energy in both plots has been scaled by the base case of $f = f_0$ and $w = w_0$. In the ΔPE plots we can notice that for the cases where Rossby number is greater than one ($1/4w_0$ (2) and $1/2w_0$ (1)) there is a very quick decay in potential energy after the initial burst. After $t = 47\text{s}(5)$ the $1/4w_0$ case has essentially no oscillations. The same is true for the $1/2w_0$ case at $t = 190\text{s}(20)$. For the other three cases with Rossby number less than one (w_0(0.5), $2w_0$(0.25), and $4w_0$(0.125)), the oscillations continue for longer times. It is also interesting to note that the most potential energy is captured within the geostrophic state for the $Ro = 1$ case. In the kinetic energy time series we see a similar result,

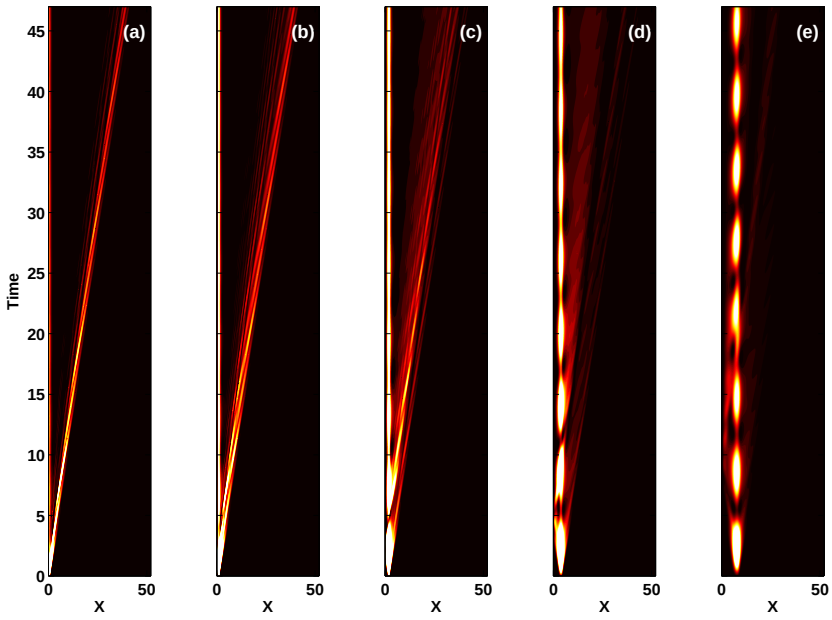

Figure 6. A space-time plot of vertically integrated kinetic energy for different values of w while f is held constant at $f = f_0$. (a) $w = \frac{1}{4}w_0$ ($Ro = 2$), (b) $w = \frac{1}{2}w_0$ ($Ro = 1$), (c) $w = w_0$ ($Ro = 0.5$), (d) $w = 2w_0$ ($Ro = 0.25$), and (e) $w = 4w_0$ ($Ro = 0.125$).

with the cases that have Rossby number larger than one decaying very quickly while the other cases continuing to oscillate for long times.

Though these two plots provide very similar information, there is one unique feature that appears in the potential energy panel: an irregularity in the steady oscillation patters for the $2w_0$ and $4w_0$ cases. These correspond to the reflected waves that were mentioned in the discussion of Fig. 6. These can be seen at $t = 952\text{s}(10)$ and $t = 238\text{s}(25)$ respectively. To investigate this further we present in Fig. 8 a space-time plot of the potential energy for the $f = f_0$, $w = w_0$ ($Ro = 0.5$) case. With this plot we can easily see the reflected wave despite not readily seeing this effect in the two previous figures. This is an extremely relevant result because the natural method of generation of waves in a tank will create waves in both directions which must be accounted for in the interpretation of physical experiments. This result is only visible in the potential energy because the amount of spanwise velocity created is so great that it drowns out this reflection signal.

We next consider how the time evolution of the total kinetic energy inside the geostrophic state compares to that outside, this is shown in Fig. 9. In this figure we have the same cases as in Fig. 7, $f = f_0$, but separated into their own plots (the panels descend from smallest initial width, $w = \frac{1}{4}w_0$ ($Ro = 2$) in (a) to largest, $w = 4w_0$ ($Ro = 0.125$) in (e)). The red line is the energy outside the geostrophic state while blue corresponds to that inside. Some immediate features are apparent from the figure: for small initial width, (a) there is more energy outside of the geostrophic state starting from an early time. The opposite

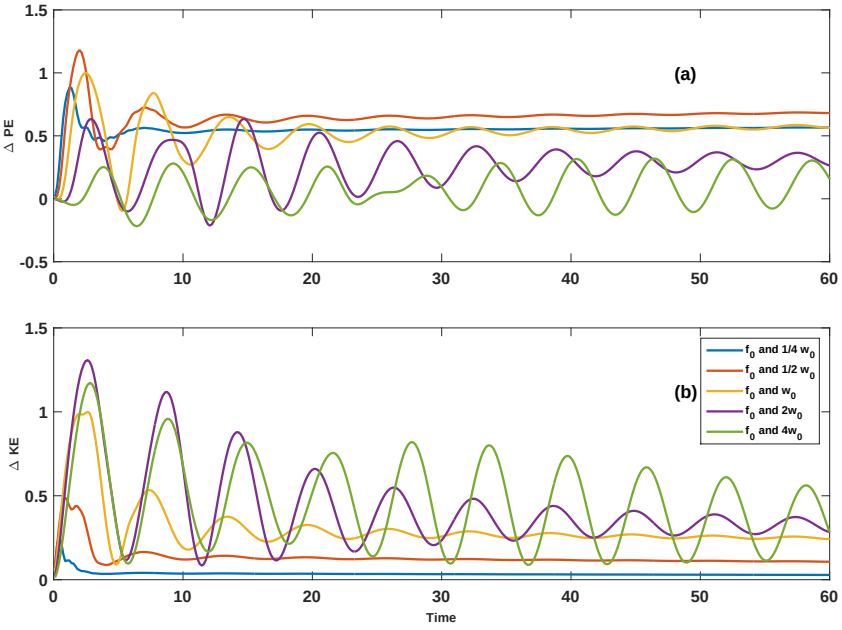

Figure 7. The changes in potential and kinetic energy, compared to the initialization, for the cases in Figure 6. (a) corresponds to the change in potential energy, while (b) to the changes in kinetic energy. The energy in both plots have been scaled by the base case ($f = f_0$, $w = w_0$).

is true for the large case, (e), where all the energy is located inside the state and very little outside. In the three intermediate cases we see that there is roughly a balance between the energy inside and outside the state, though the point where they are equal occurs later as we increase the width.

We also computed the linear kinetic energy for the geostrophic state following Boss and Thompson (1995) equation (9), using the parameter for our base case. We then compared this to the maximum kinetic energy in the geostrophic state. We calculated the linear KE should be $4.06327 \cdot 10^(-5)$ while our KE was $3.63771 \cdot 10^(-5)$ which is roughly an 11% difference.

3.4 Rossby number transition

Based on these similarities and the differences from Fig. 6, we investigate the transition region around a 'critical' Rossby number, $Ro = 1$, and how the dynamics change depending on the value ($Ro > 1$ corresponding to stronger inertia, while $Ro < 1$ to a stronger Coriolis force). Fig. 10(a) corresponds to $Ro = 1.25$ and Fig. 10(b) to $Ro = 0.75$, for both of these simulations, width was varied to change the Rossby number and f was set to f_0. There are several features which are immediately obvious: first is the shift in phase of the ejected wave packet. The packet is ejected from the front of the first pulse in the $Ro = 1.25$ case while in the $Ro = 0.75$ case the packet originates at the back of the first pulse (almost at the front of the second pulse), this was also seen in Fig. 6 when rotation rate was changed. The second feature is that the geostrophic state is significantly

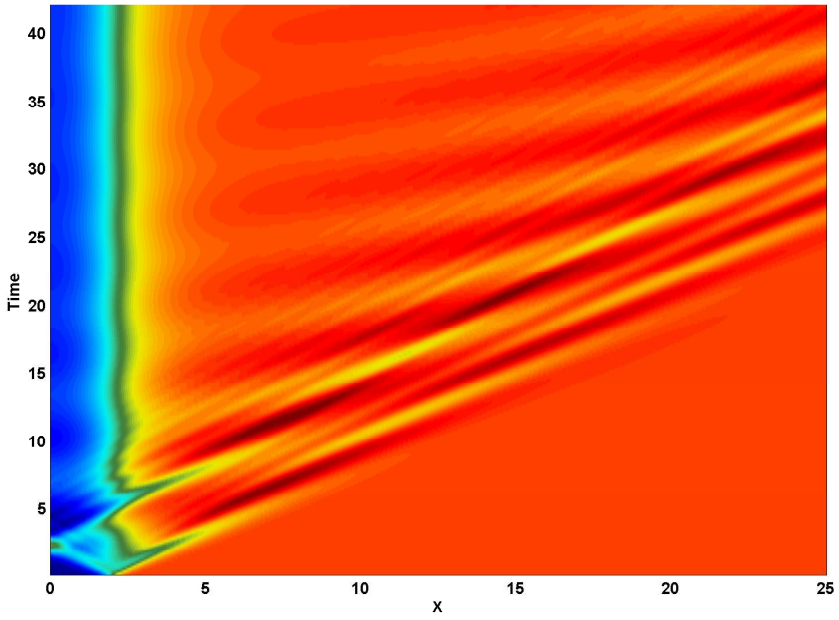

Figure 8. A space-time pseudocolour plot of the change in potential energy for our base case ($f = f_0$, $w = w_0$). It has been scaled the maximum value. From this figure it is easy to see the leftward propagating wave reflect off the left-hand wall and interact with the geostrophic state as it passes through.

wider and stronger in the $Ro = 0.75$ case. This is consistent with the idea that the Coriolis force is stronger and can trap more energy in the geostrophic state. The last feature worth noting is that in the $Ro = 0.75$ case, there is much more spreading of the wave packet as it travels through the tank. While the dynamics transitions smoothly as a function of Ro the results from this figure support the evidence seen in Fig. 6 where crossing from below to above one Rossby number corresponds to a fairly rapid change in the dynamics.

3.5 Nonlinear and polarity effects

Since the majority of classical literature on the geostrophic adjustment problem considers the linear problem, it is important to clearly identify those aspects of our simulations that are nonlinear in nature. Starting from the case with $w = \frac{1}{2}w_0$ (which was the smallest width that still produced a solitary wave), we ran several simulations where we varied the amplitude (by halving it), varied the rotation rate (which was quartered to show the clear differences), compared the different polarities and considered an extremely small amplitude 'nearly linear' case. To compare with known nonlinear wave results we computed the non-rotating version of a number of the cases. A comparison of the 1D-averaged KE for a number of the cases is presented in Fig. 11, where we have scaled any reduced amplitude cases so that, were linear theory to apply, the curves would collapse onto a single

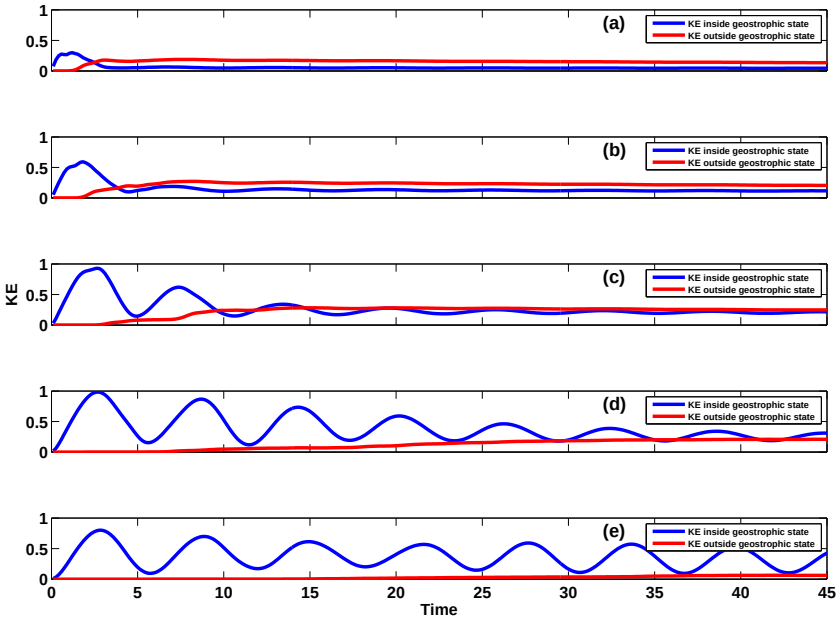

Figure 9. The total kinetic energy located inside (blue) and outside (red) of the geostrophic state. The different panels correspond to the different cases seen in Fig. 4: (a) $w = \frac{1}{4}w_0$ ($Ro = 2$), (b) $w = \frac{1}{2}w_0$ ($Ro = 1$), (c) $w = w_0$ ($Ro = 0.5$), (d) $w = 2w_0$ ($Ro = 0.25$), and (e) $w = 4w_0$ ($Ro = 0.125$).

profile. Kinetic energy was chosen as the variable shown, since it provides information about both the structure of the dynamics and magnitude of the velocities. Panel (a) shows how the non-rotating adjustment yields waves that are profoundly affected by changes in polarity, and to a lesser degree by changes in amplitude. A solitary wave train is observed for negative polarity case, and an undular bore for the positive polarity case. The change in amplitude results in a phase shift, however the amplitude of the solitary wave remains nearly constant. These results are a clear indication of nonlinear behaviour for the non-rotating case. In panel (b) we compare the same changes as panel (a), however we have included rotation and our 'nearly linear' case where the amplitude has been reduced by a factor of 200. The change in polarity does not significantly change the dynamics of the ejected waves, with the largest change between these cases being that the positive polarity case has a higher amplitude both within the wave packet and in the geostrophic state. The effect of changing the amplitude does not significantly change the wave packet, reflecting the fact that the wave packet is quite small in this case, and hence to leading order can be understood from the point of view of linear dispersive wave theory. For the geostrophic state the changes in the initial amplitude result in changes to the amplitude and the location of the peak in kinetic energy. The relationship for reduction in amplitude appears to be a greater than linear response in the amplitude of the geostrophic state. This change is most significant for the change in polarity. Linear theory, as exemplified by the green curve, provides a reasonable prediction, though details are amplitude

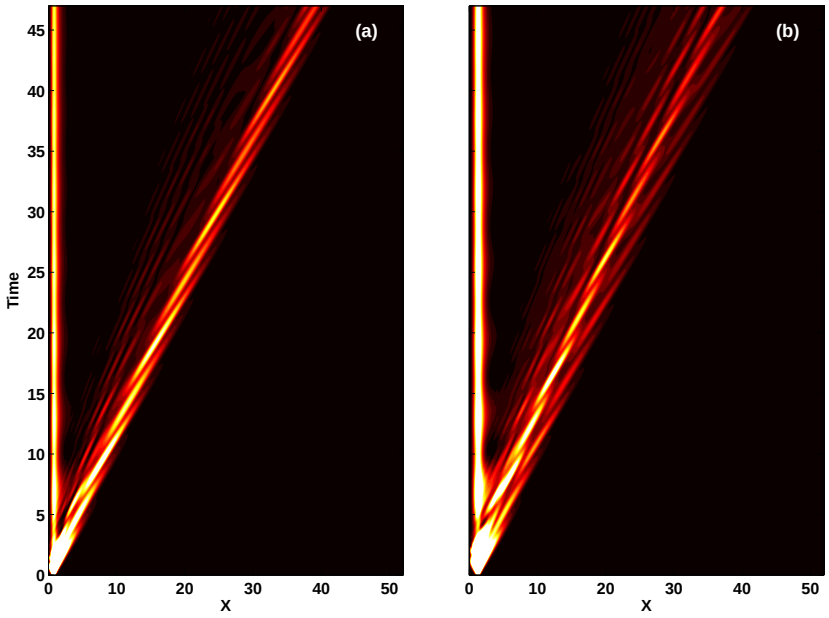

Figure 10. A space-time plot of kinetic energy for the near one Rossby number cases. (a) corresponds to the above $Ro = 1.25$ case, while (b) corresponds to the below $Ro = 0.75$ case.

dependent. For panel (c) we kept the polarity negative and compared the change in amplitude for a smaller rotation rate, as well as the non-rotating case. The lower rotation rate allows for more energy to be deposited into the wave train, with a nonlinear wave packet-like behaviour. The primary change for the reduction in amplitude is that the individual waves within the wave packet of the scaled reduced case (in blue) appear to be larger in amplitude compared to the base case (in black). There also appears to be a slight phase shift between the cases. Comparing these two cases to the non-rotating case shows that while the peak in energy has been shifted back, the wave front of the solitary wave and the wave packets are at roughly the same location. In contrast to what was observed before, for the lower rotation case there is very little difference in the geostrophic state as a result of amplitude reduction, implying that for low rotation rates the geostrophic state can be well-described by linear theory. The results presented in Fig. 11 indicate that for this problem changes in polarity are the dominant nonlinear effect and that depending on the rotation parameter nonlinear effects will either be seen in the geostrophic state or in the wave packet.

To investigate the nonlinear effects that arise from changes in polarity in the geostrophic state (Fig. 11(b)), long-time simulations with a rotation rate set to $f = 2f_0$ and an initial width of $w = \frac{1}{2}w_0$ were computed, resulting in a Rossby number of $\frac{1}{2}$. These results are presented in Fig. 12. Panels (a) and (b) show the vertically integrated kinetic energy at the centre of kinetic energy in the geostrophic state. (c) and (d) show the total normalized kinetic energy around the geostrophic state, along with contours of constant density, for a negative and positive initial polarity respectively. Panel (a) clearly shows the energy

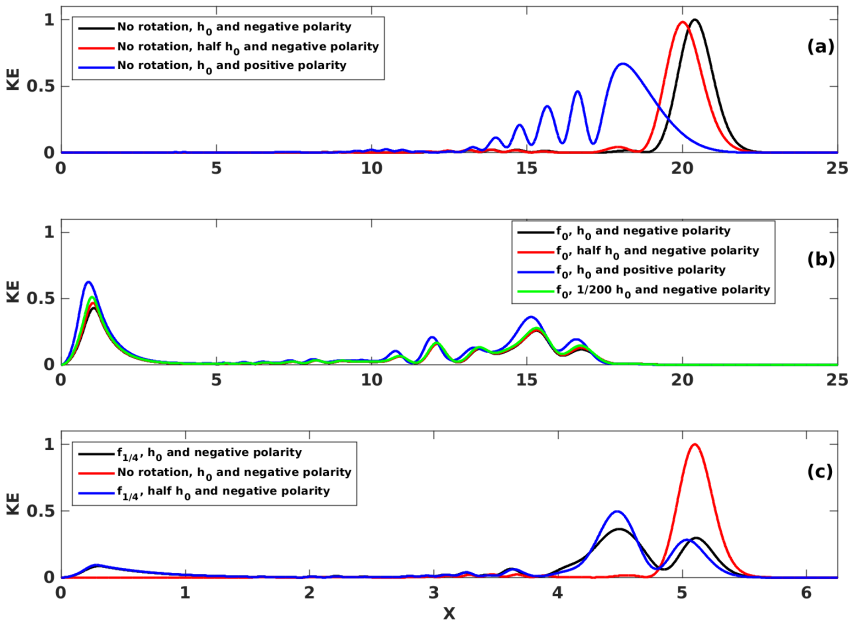

Figure 11. A comparison of the 1D KE for several different cases to outline the effects of non-linearity. All plots are taken at $t = 240$s(1140 for the non-rotating case, 25.2 for the f_0 case and 6.3 for the $\frac{1}{4}f_0$ case) and have been scaled by the change in amplitude squared. The kinetic energy has also been normalized by the maximum of the non-rotating negative polarity case. (a) highlights the differences that arise from halving the initial amplitude and by changing the polarity of the non-rotating case. (b) compares the same changes as the panel above, however we have included rotation, and also consider a 'nearly linear' case with an initial amplitude of $1/200\eta_0$. (c) is a comparison of different negative polarity cases, one with no rotation and the standard amplitude, and two others at $\frac{1}{4}f_0$ with standard and half amplitude.

difference that was seen in Fig. 11(b), indicating that the positive polarity case appears more efficient at keeping energy in the geostrophic state. Panel (b) shows the time series of the logarithm of kinetic energy after the packet has been ejected. If we ignore the inertial oscillations, which appear to be rapid on the time scale shown, we can see a clear decay. From this panel it is also possible to note that the oscillations appear to persist significantly longer in the positive case. By computing the logarithm of the time series (Fig. 11(b)) we are able to show that the decay is nearly exponential, with the positive polarity case decaying roughly 5% faster. The decay rate decreases over time. From the bottom two panels, (c) and (d), it is clear that the polarity of the geostrophic state strongly modifies the vertical distribution of the kinetic energy in the geostrophic state.

We now consider the effect that polarity has on the wave train ejected from the geostrophic state. We also consider both a high ($f = 2f_0$) and low ($f = \frac{1}{8}f_0$) rotation rate. In all cases the initial width is set to $w = \frac{1}{2}w_0$ (so $Ro = 0.5$ and $Ro = 8$ respectively). The density contours of these cases are shown in Fig. 13. We see that there are substantial differences between the polarities in the low ($f = \frac{1}{8}f_0$) rotation case, (a) and (b). Despite having rotation, we obtain a result that at least bears some resemblance to the non-rotating case. This changes substantially when we consider the high ($f = 2f_0$) rotation case (c) and

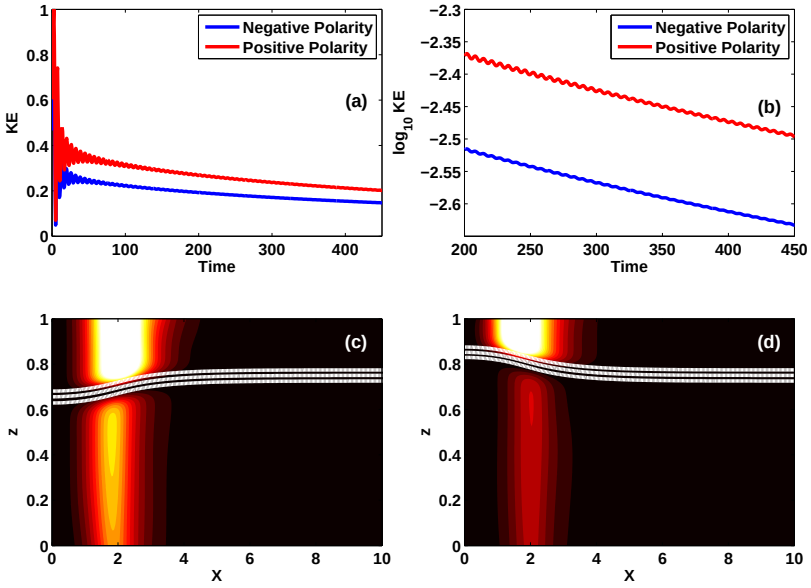

Figure 12. Long time simulations contrasting negative (left column) and positive polarity (right column) geostrophic states. $f = 2f_0$, $w = \frac{1}{2}w_0$ and $Ro = \frac{1}{2}$. (a) presents the long-time time-series of vertically integrated kinetic energy in the geostrophic state. (b) shows the base ten logarithm of the geostrophic state kinetic energy after the packet has been ejected. (c) and (d) show the shaded distribution of kinetic energy in the geostrophic state, along with contours of constant density, for a negative and positive initial polarity respectively.

(d). In these panels the two cases are almost indistinguishable from each other. An important difference to notice between the high and low rotation cases is that the amplitude of the ejected waves is significantly reduced. We argue that this collapse of the different polarities into the same dynamics for higher rotation rates is a result of the geostrophic state capturing more energy, resulting in smaller amplitude waves being ejected and thus decreasing the effect of non-linearity.

To investigate the transition from distinct to uniform dynamics of the wave trains, we examined the differences in spectra (again based on the 1D vertically integrated kinetic energy) of the ejected waves for the low rotation rate from the previous figure and the case of no rotation. This is presented in Fig. 14. Fig. 14(a) corresponds an initial wave of elevation, and Fig. 14(b) to one of depression. In the case of an initial elevation, we can see that when rotation is introduced, the power at specific wave numbers is increased. A similar observation can be made based for Fig. 14(b), in which the Gaussian-like profile typical of a solitary wave is destroyed by rotation, and replaced by peaks at specific wave numbers. These results suggest that a spectral analysis will reveal the results of rotation equally well for both polarities. This is important since the solitary wave case (in the absence of rotation) can be described quite succinctly, but the undular bore spreads spatially with increasing time. We further considered the spectra of the waves for a higher rotation cases and found that as the rotation rate was increased (Rossby

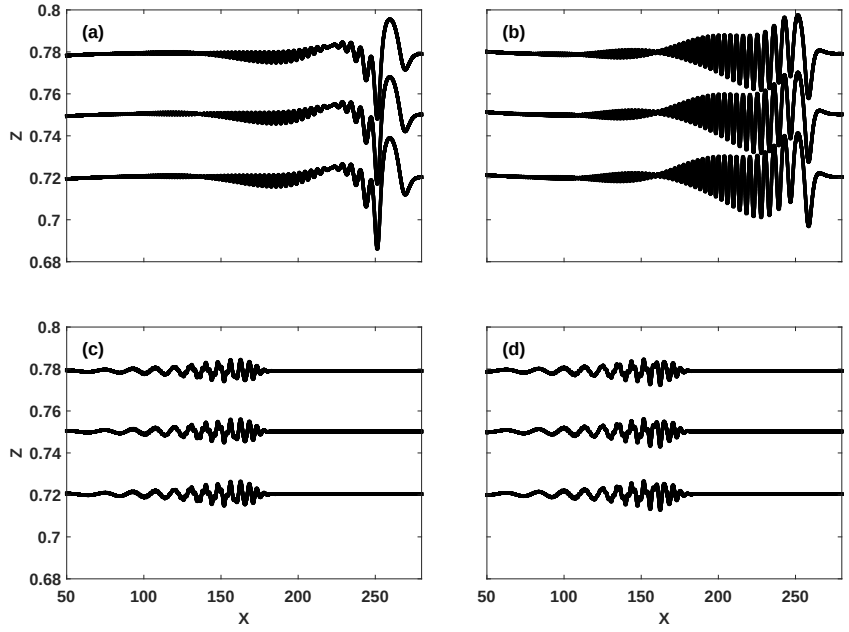

Figure 13. A series of comparisons of the density field across two different rotation rates, $f = 2f_0$ ($Ro = 0.5$) and $f = \frac{1}{8}f_0$ ($Ro = 8$) and the two polarities. All the cases initially start with $w = \frac{1}{2}w_0$. (a) corresponds to $f = \frac{1}{8}f_0$ and negative polarity, (b) to $f = \frac{1}{8}f_0$ and positive polarity, (c) to $f = 2f_0$ and negative polarity and (d) to $f = 2f_0$ and positive polarity.

number decreased) the differences in polarity become negligible, in agreement with the discussion above, and the results shown in Fig. 13.

4 Conclusions

In this paper we have taken a systematic approach to the classical rotation-modified stratified adjustment problem. Building on results based on shallow water theory presented in Kuo and Polvani (1997), we have shown that by using the fully nonlinear Euler equations the waves that are ejected from the geostrophic state do not steepen to a shock. By mapping out the parameter space we have shown that, as expected, the Rossby number is the controlling variable for the dynamics in this problem. When the Rossby number is well above one, a wave packet is ejected from the first inertial wave pulse of the geostrophic state, and does not disperse much as it propagates through the tank. When the Rossby number is less than one, the packet is ejected from a later pulse (smaller Rossby numbers corresponding to later pulses), and disperses as it moves through the tank. The transition between the two cases is continuous but clearly evident when contrasting a case with $Ro = 0.75$ and one with $Ro = 1.25$. We characterized the similarities and differences in the dynamics for cases when the same Rossby number is achieved by different means. We found that for the same Rossby number the dynamics of the geostrophic state are nearly identical, though

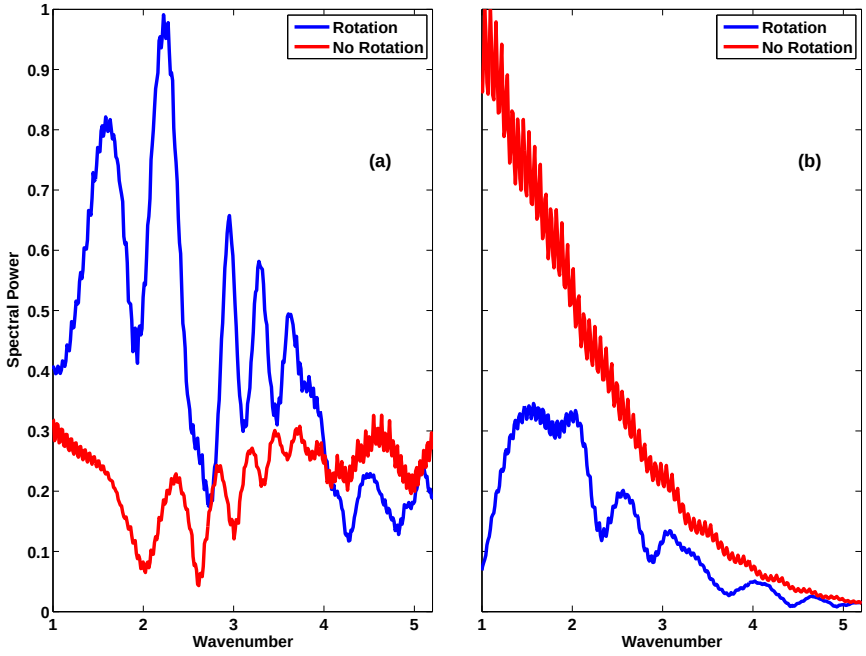

Figure 14. Comparison of the scaled filtered spectra based on the 1D vertically integrated kinetic energy, for no rotation and $f = \frac{1}{8} f_0$ ($Ro = 8$), where (a) corresponds to an initial wave of elevation and (b) corresponds to an initial wave of depression. This figure is taken at 2250s (29.5 in the rotating case and 236.8 in the non rotating case) and the initial width is $w = \frac{1}{2} w_0$. The spectra have been scaled by the maximum value between the cases and the wave number has been scaled by $\frac{2\pi}{Ro_r}$.

there are some small differences between the wave trains. Our results show that the oscillations in the geostrophic state can persist for long times, in agreement with Kuo and Polvani (1997). In cases with $Ro \leq \frac{1}{8}$, almost all the energy in the system is trapped within the geostrophic state. The effects of nonlinearity were investigated by considering different initial amplitudes and changes in polarity. As in the non-rotating case, the largest nonlinear effects occurred as a result of changes in polarity, both in the geostrophic state and in the wave packet ejected. High (low) Rossby numbers yielded nonlinear effects in the wave train (geostrophic state). Amplitude effects were smaller than polarity effects. For the wave train, we demonstrated that the nonlinear wave packet interpretation of the wave train of Grimshaw et al. (2012) is appropriate in some parameter regimes, with changes in amplitude reflected in the phase of the nearly solitary wave response. The characterization of these various nonlinear effects in a single simulation is new and significant, providing a guideline for when linear theory can be applied, and when nonlinear effects must be considered. A second significant finding presented is the generation, reflection and interaction of a wave train propagating in the opposite direction (leftward) during the initial generation. For any physical tank set up, this reflected wave will impact any measurements of the waves generated and especially any measurements of the geostrophic state. By extending the spatial extent of the simulation and letting the system evolve for a longer time, we have shown that the wave

packet at the front of the wave train does not separate from the tail, which is in contrast to the results predicted by Helfrich (2007). We argue that model equations, such as the Ostrovsky equations, while useful for describing qualitative aspects of the wave train, miss significant aspects of the full dynamics.

While the main focus of this work is to build on the nonlinear wave literature (for which the assumption of a constant buoyancy frequency is a pathological limit), it is worth noting that geostrophic adjustment has been considered via a very different technique in the literature. Sundermeyer and Lelong (2005) performed three-dimensional simulations of a triply-periodic, linearly stratified domain. Energy was injected into the system via local patches of diffusivity, and the resulting state was allowed to adjust. The authors found that vortex–vortex interactions drive strong nonlinearity, albeit after a period of adjustment that is many inertial periods long. The detailed dynamics of the adjustment period is not considered in detail, and in any event the physical scales of the study are chosen so that our model tank would span less than 5 grid points, and hence detailed comparisons would be premature. However, an extension of the present work to the collapse of an initially mixed region and the generation of higher mode waves could provide an interesting bridge between these two presently divergent research directions.

In addition to the work described in the previous paragraph, future work should consider spanwise variations, especially in the case of the strong geostrophic state for which novel instabilities may be possible. Systematic studies of the shoaling of rotation-modified solitary waves and undular bores should also be carried out, since it is not known in what manner these may be different from shoaling in the non-rotating case. A more theoretical avenue could quantitatively compare weakly nonlinear and weakly dispersive-strongly nonlinear model equations to the full stratified equations.

This research was supported by the Natural Sciences and Engineering Research Council of Canada.

References

Boss, E. and Thompson, L.: Energetics of Nonlinear Geostrophic Adjustment, Journal of Physical Oceanography, 25, 1521–1529, doi:10.1175/1520-0485(1995)025<1521:EONGA>2.0.CO;2, https://www.researchgate.net/publication/232711566{_}Energetics{_}of{_}Nonlinear{_}Geostrophic{_}Adjustment, 1995.

Cahn, A.: An Investigation of the Free Oscillations of a Simple Current System, Journal of Meteorology, 2, 113–119, doi:10.1175/1520-0469(1945)002<0113:AIOTFO>2.0.CO;2, http://journals.ametsoc.org/doi/abs/10.1175/1520-0469(1945)002{%}3C0113:AIOTFO{%}3E2.0.CO{%}3B2, 1945.

Carr, M. and Davies, P. A.: The motion of an internal solitary wave of depression over a fixed bottom boundary in a shallow, two-layer fluid, Physics of Fluids, 18, 016 601, doi:10.1063/1.2162033, http://scitation.aip.org/content/aip/journal/pof2/18/1/10.1063/1.2162033, 2006.

Gerkema, T., Zimmerman, J. T. F., Maas, L. R. M., and van Haren, H.: Geophysical and astrophysical fluid dynamics beyond the traditional approximation, Reviews of Geophysics, 46, RG2004, doi:10.1029/2006RG000220, http://doi.wiley.com/10.1029/2006RG000220, 2008.

Gill, A.: Atmosphere-ocean dynamics, Academic press, https://books.google.ca/books?hl=en{&}lr={&}id=8kFPh{_}SvnAIC{&}oi=fnd{&}pg=PP1{&}dq=Atmosphere+Ocean+dynamics+Gill{&}ots=B82Q2v1Umm{&}sig=eN5ANYnstDvva2w2fLdWLKGHgaA, 1982.

Gill, A. E.: Adjustment under gravity in a rotating channel, Journal of Fluid Mechanics, 77, 603–621, doi:10.1017/S0022112076002280, http://journals.cambridge.org/abstract{_}S0022112076002280, 1976.

Grimshaw, R. and Helfrich, K.: Longtime Solutions of the Ostrovsky Equation, Studies in Applied Mathematics, 121, 71–88, http://onlinelibrary.wiley.com/doi/10.1111/j.1467-9590.2008.00412.x/full, 2008.

Grimshaw, R. H. J., Ostrovsky, L. A., Shrira, V. I., and Stepanyants, Y. A.: Long Nonlinear Surface and Internal Gravity Waves in a Rotating Ocean, Surveys in Geophysics, 19, 289–338, doi:10.1023/A:1006587919935, 1998.

Grimshaw, R. H. J., Helfrich, K., and Johnson, E. R.: The Reduced Ostrovsky Equation: Integrability and Breaking, Studies in Applied Mathematics, 129, 414–436, doi:10.1111/j.1467-9590.2012.00560.x, 2012.

Grimshaw, R. H. J., Helfrich, K. R., and Johnson, E. R.: Experimental study of the effect of rotation on nonlinear internal waves, Physics of Fluids, 25, 056 602, doi:10.1063/1.4805092, http://scitation.aip.org/content/aip/journal/pof2/25/5/10.1063/1.4805092, 2013.

Grue, J., Jensen, A., Rusås, P.-O., and Sveen, J. K.: Breaking and broadening of internal solitary waves, Journal of Fluid Mechanics, 413, 181–217, doi:10.1017/S0022112000008648, http://journals.cambridge.org/abstract{_}S0022112000008648, 2000.

Helfrich, K. R.: Decay and return of internal solitary waves with rotation, Physics of Fluids, 19, 026 601, doi:10.1063/1.2472509, http://scitation.aip.org/content/aip/journal/pof2/19/2/10.1063/1.2472509, 2007.

Helfrich, K. R. and Melville, W. K.: Long Nonlinear Internal Waves, Annual Review of Fluid Mechanics, 38, 395–425, doi:10.1146/annurev.fluid.38.050304.092129, http://www.annualreviews.org/doi/abs/10.1146/annurev.fluid.38.050304.092129, 2006.

Johnson, R.: A modern introduction to the mathematical theory of water waves, Cambridge University Press, vol 19. edn., https://books.google.ca/books?hl=en{&}lr={&}id=oQ2Cw4Rnve8C{&}oi=fnd{&}pg=PR11{&}dq=A+Modern+Introduction+to+the+Mathematical+Theory+of+Water+Waves{&}ots=VaS8poLlKZ{&}sig=J1xxQgUPX4GiJvG94uZhAu0uFuc, 1997.

Killworth, P. D.: The Time-dependent Collapse of a Rotating Fluid Cylinder, Journal of Physical Oceanography, 22, 390–397, doi:10.1175/1520-0485(1992)022<0390:TTDCOA>2.0.CO;2, http://journals.ametsoc.org/doi/abs/10.1175/1520-0485(1992)022{%}3C0390:TTDCOA{%}3E2.0.CO;2, 1992.

Kuo, A. and Polvani, L.: Time-dependent fully nonlinear geostrophic adjustment, Journal of physical oceanography, 27, 1614–1634, doi:10.1175/1520-0485(1997)027<1614:TDFNGA>2.0.CO;2, http://journals.ametsoc.org/doi/full/10.1175/1520-0485(1997)027{\T1\textless}1614:TDFNGA{\T1\textgreater}2.0.CO;2, 1997.

Kuo, A. C. and Polvani, L. M.: Wave–vortex interaction in rotating shallow water. Part 1. One space dimension, Journal of Fluid Mechanics, 394, 1–27, 1999.

Lamb, K.: Particle transport by nonbreaking, solitary internal waves, Journal of Geophysical Research: Oceans, 102, 18 641–18 660, http://onlinelibrary.wiley.com/doi/10.1029/97JC00441/full, 1997.

Lamb, K. and Nguyen, V.: Calculating energy flux in internal solitary waves with an application to reflectance, Journal of Physical Oceanography, 39, 559–580, http://journals.ametsoc.org/doi/abs/10.1175/2008JPO3882.1, 2009.

Middleton, J. F.: Energetics of Linear Geostrophic Adjustment, Journal of Physical Oceanography, 17, 735–740, doi:10.1175/1520-0485(1987)017<0735:EOLGA>2.0.CO;2, http://journals.ametsoc.org/doi/abs/10.1175/1520-0485(1987)017{%}3C0735:EOLGA{%}3E2.0.CO;2, 1987.

Mihaljan, J.: The exact solution of the Rossby adjustment problem, Tellus A, http://tellusa.net/index.php/tellusa/article/download/8833/10293, 1963.

Ou, H. W.: Geostrophic Adjustment: A Mechanism for Frontogenesis, Journal of Physical Oceanography, 14, 994–1000, doi:10.1175/1520-0485(1984)014<0994:GAAMFF>2.0.CO;2, http://journals.ametsoc.org/doi/abs/10.1175/1520-0485(1984)014{%}3C0994:GAAMFF{%}3E2.0.CO;2, 1984.

Rossby, C.: On the mutual adjustment of pressure and velocity distributions in certain simple current systems, J. Mar. Res, 1, 239–263, http://www.aos.princeton.edu/WWWPUBLIC/gkv/history/Rossby-adj38.pdf, 1937.

Stastna, M., Poulin, F. J., Rowe, K. L., and Subich, C.: On fully nonlinear, vertically trapped wave packets in a stratified fluid on the f-plane, Physics of Fluids, 21, 106 604, doi:10.1063/1.3253400, http://link.aip.org/link/PHFLE6/v21/i10/p106604/s1{&}Agg=doi, 2009.

Subich, C. J., Lamb, K. G., and Stastna, M.: Simulation of the Navier-Stokes equations in three dimensions with a spectral collocation method, International Journal for Numerical Methods in Fluids, 73, 103–129, doi:10.1002/fld.3788, http://doi.wiley.com/10.1002/fld.3788, 2013.

Sundermeyer, M. A. and Lelong, M.-P.: Numerical Simulations of Lateral Dispersion by the Relaxation of Diapycnal Mixing Events, Journal of Physical Oceanography, 35, 2368–2386, doi:10.1175/JPO2834.1, http://journals.ametsoc.org/doi/abs/10.1175/JPO2834.1, 2005.

Washington, W. M.: A note on the adjustment towards geostrophic equilibrium in a simple fluid system, Tellus, 16, 530–534, doi:10.1111/j.2153-3490.1964.tb00189.x, http://tellusa.net/index.php/tellusa/article/view/8985, 1964.

Zeitlin, V., Medvedev, S. B., and Plougonven, R.: Frontal geostrophic adjustment, slow manifold and nonlinear wave phenomena in one-dimensional rotating shallow water. Part 1. Theory, Journal of Fluid Mechanics, 481, 269–290, doi:10.1017/S0022112003003896, http://www.journals.cambridge.org/abstract{_}S0022112003003896, 2003a.

Zeitlin, V., Reznik, G. M., and Jelloul, M. B.: Nonlinear theory of geostrophic adjustment. Part 2. Two-layer and continuously stratified primitive equations, Journal of Fluid Mechanics, 491, 207–228, doi:10.1017/S0022112003005457, http://www.journals.cambridge.org/abstract{_}S0022112003005457, 2003b.

Table 1. Rossby number of each simulation, where $f_0 = 0.105\text{s}^-1$ and w_0=1.63m.

Ro	$\frac{1}{4}w_0$	$\frac{1}{2}w_0$	w_0	$2w_0$	$4w_0$
f_0	2	1	$\frac{1}{2}$	$\frac{1}{4}$	$\frac{1}{8}$
$\frac{1}{2}f_0$	4	2	1	$\frac{1}{2}$	$\frac{1}{4}$
$\frac{1}{4}f_0$	8	4	2	1	$\frac{1}{2}$

Table 2. Reynolds number of each simulation, where $f_0 = 0.105\text{s}^{-1}$ and w_0=1.63m.

Re	$\frac{1}{4}w_0$	$\frac{1}{2}w_0$	w_0	$2w_0$	$4w_0$
f_0	$3.495 \cdot 10^4$	$6.990 \cdot 10^4$	$1.398 \cdot 10^5$	$2.796 \cdot 10^5$	$5.593 \cdot 10^5$
$\frac{1}{2}f_0$	$3.495 \cdot 10^4$	$6.990 \cdot 10^4$	$1.398 \cdot 10^5$	$2.796 \cdot 10^5$	$5.593 \cdot 10^5$
$\frac{1}{4}f_0$	$3.495 \cdot 10^4$	$6.990 \cdot 10^4$	$1.398 \cdot 10^5$	$2.796 \cdot 10^5$	$5.593 \cdot 10^5$